

FULL PAPER

Open Access



Focal mechanisms and stress field in the Nobi fault area, central Japan

Kei Katsumata^{1*}, Masahiro Kosuga², Hiroshi Katao³, Takuji Yamada^{1,5}, Aitaro Kato⁴ and the Research Group for the Joint Seismic Observations at the Nobi Area

Abstract

In this study, we obtained 728 focal mechanisms of small earthquakes with depths shallower than 20 km that occurred from May 2009 to May 2013 in the Nobi fault area in central Japan. The averages of the azimuths of the P- and T-axes were $N97^\circ \pm 23^\circ$ E and $N6^\circ \pm 32^\circ$ E, and the averages of the dips of the P- and T-axes were $11^\circ \pm 10^\circ$ and $32^\circ \pm 25^\circ$, respectively. These variations in the P- and T-axes come from variation of the focal mechanisms; both strike-slip and reverse fault earthquakes were observed in the study area. A stress tensor inversion method was applied to the focal mechanisms, and we obtained and characterized the spatial pattern of the tectonic stress. We found that the maximum principal stress (σ_1) is oriented E–W over almost the entire study area. The stress ratio R , which is defined as $R = (\sigma_1 - \sigma_2)/(\sigma_1 - \sigma_3)$, ranges from 0.65 to 0.98, and the average R over the entire study area is 0.82. The average stress ratio is close to unity, indicating $\sigma_2 \approx \sigma_3$, and thus the dominant stress in this region is a uniaxial compression in the direction of σ_1 . The direction of the σ_1 -axis fluctuates locally at the southeastern end of the seismic fault ruptured by the 1891 Nobi earthquake. This fluctuation is limited to within a very narrow zone across the seismic fault in the upper crust shallower than approximately 10 km, suggesting that most of the deviatoric stress at the southeastern end of the seismic fault ruptured by the 1891 Nobi earthquake was not released.

Keywords: Nobi fault system; Nobi earthquake; Focal mechanism; Stress tensor inversion; Intraplate earthquake; Active fault

Background

The Nobi earthquake, which occurred in 1891 in central Japan, resulted in the death of more than 7,000 people and the complete destruction of more than 140,000 houses (Milne 1893). This is the largest earthquake on record in the shallow crust of the inland area of Japan. Its magnitude was determined to be 8.0 by the Japan Meteorological Agency (JMA) and the U.S. Geological Survey. The seismic moment of this event was 1.8×10^{20} Nm, which corresponds to $M_w = 7.5$ (Fukuyama et al. 2007). A 76-km-long surface trace was found, and the maximum surface displacement was 7 m left laterally and 6 m vertically (Matsuda 1974). The Nobi fault system strikes in the NW–SE direction and consists of three major faults: the Nukumi fault in its northwestern part, the Neodani fault in its central part, and the Umehara

fault in its southeastern part (Fig. 1). According to trench studies, all of these faults exhibit repetitive left-lateral strike-slip faulting; however, these three faults have not always ruptured simultaneously. The average recurrence times of the Neodani and Umehara faults are 2700 years and more than 11,000 years, respectively (Awata et al. 1999). Historically, the Tenpyo earthquake in 745 and the Tensho earthquake in 1586 may have occurred in central Japan and had magnitudes as large as that of the 1891 Nobi earthquake. Although the details of these two historical earthquakes are unknown, large intraplate earthquakes have continued to occur in central Japan.

The region of the Eurasian plate containing central Japan is compressed by both the Philippine Sea (PH) plate from the south and the Pacific (PA) plate from the east (Fig. 1). The PH plate and PA plate are subducting beneath the Nankai Trough and Japan Trench, respectively. Although it is clear that the tectonic stress due to the subduction of the two plates is loaded on intraplate faults in central Japan, the detailed mechanism of the

* Correspondence: kkatsu@mail.sci.hokudai.ac.jp

¹Institute of Seismology and Volcanology, Hokkaido University, Sapporo 060-0810, Japan

Full list of author information is available at the end of the article

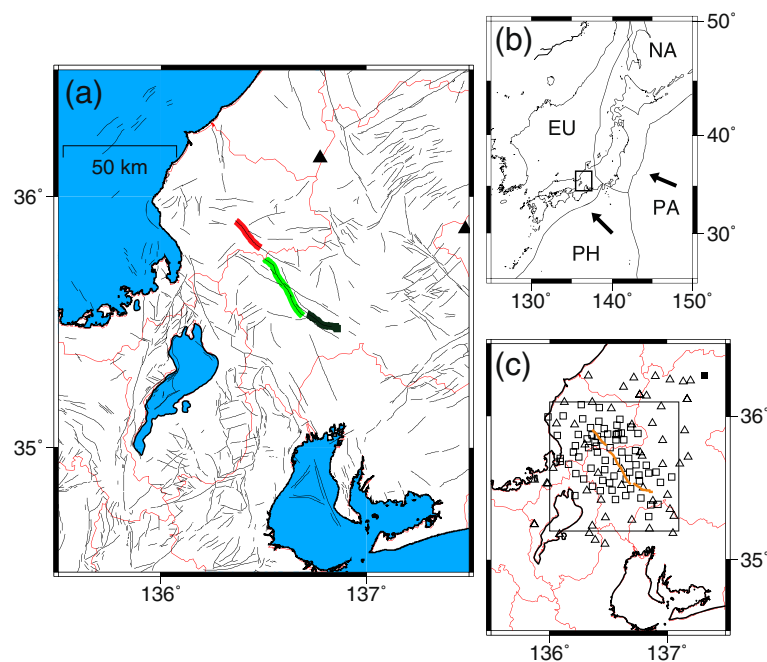


Fig. 1 Map showing the Nobi fault area. **a** Bold orange, green, and blue lines are the Nukumi, Neodani, and Umehara faults, respectively. Thin lines are other active faults. Closed triangles show active volcanoes. Red lines show political prefecture boundaries. **b** Study area and plate configuration. PA: Pacific plate, PH: Philippine Sea plate, EU: Eurasian plate, and NA: North American plate. The two arrows indicate plate motions of PA and PH relative to EU. **c** Temporary and permanent seismographic stations used in this study are indicated by open squares and open triangles, respectively. The rectangle indicates the area shown in Fig. 3

stress accumulation is still debated. Two models for the occurrence of the intraplate earthquakes have been proposed recently. Kawanishi et al. (2009) named the two models the regional stress model and the local stress model. The difference between these models is whether or not the tectonic stress due to the subduction of the plates is locally concentrated on the intraplate earthquake faults. The regional stress model assumes that the stress builds up uniformly in a broad area that includes the intraplate earthquake faults (e.g., Sykes 1978; Hinze et al. 1988; Johnston and Kanter 1990; Zoback 1992). Conversely, the local stress model assumes that the stress is locally concentrated on the intraplate earthquake faults (e.g., Campbell 1978; Liu and Zoback 1997; Stuart et al. 1997). To investigate which model is plausible, the spatial pattern of the stress field is of importance.

The first purpose of this study was to obtain precise focal mechanisms in the Nobi fault area using *P*-wave first-motion data collected by temporary seismic observation. The second purpose was to obtain and characterize the spatial pattern of the stress field based on the focal mechanisms.

Methods

To obtain a comprehensive understanding of the mechanism of the stress accumulation, a temporary observation was conducted in and around the Nobi fault system

in central Japan from 2009 to 2013 by the Research Group for the Joint Seismic Observations at the Nobi Area, which consists of Hokkaido University, Hirosaki University, Tohoku University, the University of Tokyo, Nagoya University, Kyoto University, Kyushu University, Kagoshima University, and the National Research Institute for Earth Science and Disaster Prevention. A total of 70 temporary seismographic stations were deployed in an area of 100×100 km that includes the Nobi fault system (Fig. 1). The temporary seismographic stations consisted of 45 telemetry online systems and 25 portable offline systems. A three-component seismograph with a natural frequency of 1 Hz was installed at each station. Fifty-three permanent online seismographic stations in and around the temporary seismic network were also used in this study.

We determined hypocenters by using HYPOMH, which is based on a simple maximum-likelihood estimation algorithm with a Bayesian approach (Hirata and Matsu'ura 1987). We assumed a one-dimensional *P*-wave velocity structure, as shown in Fig. 2 (Ito and Wada 2002), which is the same as that used for the hypocenter calculation at the Kamitakara Seismic Observatory of Kyoto University (KTJ), located in central Japan. The *S*-wave velocity was obtained by the relationship $V_P/V_S = \sqrt{3}$, where V_P and V_S are the *P*- and *S*-wave velocities, respectively. This assumption is equivalent to assuming a Poisson's ratio of

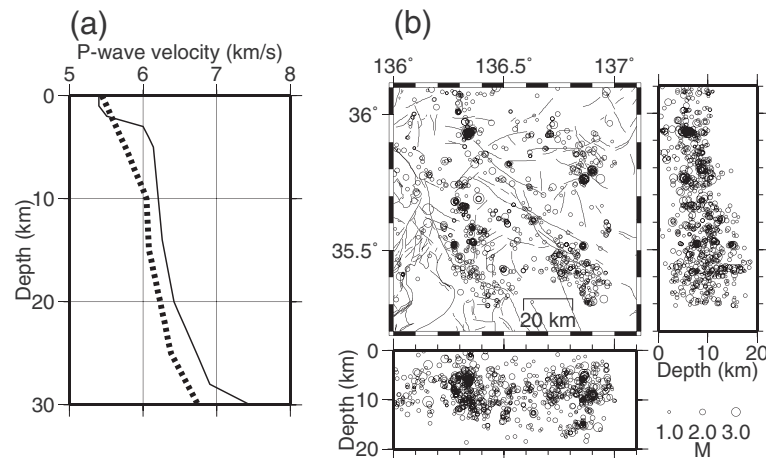


Fig. 2 **a** Assumed velocity structure of *P*-wave. Solid line indicates the structure used for routine hypocenter determination at Kamitakara Seismic Observatory, Kyoto University (Ito and Wada 2002). Broken line indicates the structure based on seismic tomography (Nakajima et al. 2014). **b** Earthquake hypocenters. Between May 2009 and May 2013, we located 890 events in the study area

0.25, which is often applied to crustal structures. We located 890 earthquakes in the study area (35.3–36.1° N, 136.0–137.0° E), observed from May 2009 to May 2013, with depths shallower than 20 km and magnitudes ranging from 1.0 to 4.6 (Fig. 2). The hypocenters are distributed homogeneously in the study area rather than being concentrated in a limited region.

P-wave first-motion polarities were selected manually by careful inspection. To determine the focal mechanisms, we applied the HASH program (Hardebeck and Shearer 2002) to the polarity data. No amplitude data were used. HASH uses a grid-search technique to find a set of acceptable focal mechanisms. During the grid-search process, the increment angle for the strike, dip, and rake of the focal mechanism is set at 5°. HASH can determine the focal mechanism if an earthquake satisfies the following three conditions associated with station coverage: (1) the number of polarity data points is more than 8, (2) the maximum azimuthal gap is smaller than 90° on the focal sphere, and (3) the maximum takeoff angle gap is smaller than 60°. An acceptable set of solutions is selected among trial solutions computed by varying earthquake location and velocity structure. The depth of the hypocenter was selected randomly from a normal distribution based on the calculation error reported by HYPOMH. The average horizontal and vertical errors were ± 0.1 and ± 0.2 km, respectively. To estimate the uncertainty of the takeoff angle, we assumed the two velocity structures shown in Fig. 2. One is the structure used at KTJ in this study, and the other is that from Nakajima et al. (2014) based on seismic tomography. The spread of the acceptable mechanisms determines the uncertainty and the solution quality. We obtained 728 focal mechanisms in the study area (Fig. 3). An additional data file shows these focal mechanisms in

more detail (see Additional file 1). The number of polarity data points ranged from 11 to 165. Of the obtained focal mechanisms, 99 were determined using more than 100 *P*-wave polarity data points, and 664, which is 90 % of the total, were determined using more than 30 *P*-wave polarity data points. The fault plane uncertainty ranged from 7° to 47°, and the average uncertainty for the 1456 ($=728 \times 2$) fault planes of the 728 focal mechanisms was $26^\circ \pm 7^\circ$. Hardebeck and Shearer (2002) defined the

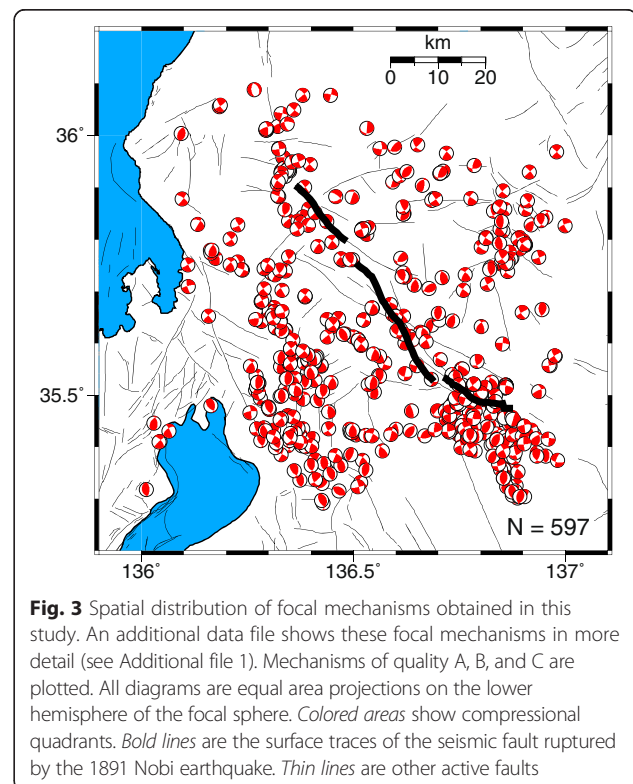


Fig. 3 Spatial distribution of focal mechanisms obtained in this study. An additional data file shows these focal mechanisms in more detail (see Additional file 1). Mechanisms of quality A, B, and C are plotted. All diagrams are equal area projections on the lower hemisphere of the focal sphere. Colored areas show compressional quadrants. Bold lines are the surface traces of the seismic fault ruptured by the 1891 Nobi earthquake. Thin lines are other active faults

quality of solutions as quality A, B, C, or D, where quality A and D solutions have the highest and lowest levels of quality, respectively. In this study, we obtained 127, 231, 239, and 131 focal mechanisms of quality A, B, C, and D, respectively. We use the 597 focal mechanisms of quality A, B, and C for the remainder of this study. The fault plane uncertainty of these mechanisms ranges from 7° to 43°, and the average for the 1194 ($=597 \times 2$) fault planes of the 597 focal mechanisms is $24^\circ \pm 7^\circ$.

To produce a regional scale model of the stress orientation, we applied a stress tensor inversion method to the focal mechanisms obtained by the HASH technique. The method used in this study is the Spatial And Temporal Stress Inversion (SATSI) method developed by Hardebeck and Michael (2006), which is a modified version of the code by Michael (Michael 1987). In the SATSI method, the study area is divided into small subareas, and a damped inversion method is applied to simultaneously invert for stress in all subareas while minimizing the difference between the stresses of adjacent subareas. The uncertainty of the stress orientation is estimated using 2000 bootstrap resampling of all data (Hardebeck and Michael 2006). The 1-sigma confidence region of the stress model is defined by the 68 % of the bootstrap solutions closest to the preferred solution. To investigate the spatial change in the stress field, we divided the focal mechanisms into four groups according to their focal depths and calculated the spatial distribution of the stress field in each group using the SATSI method. Almost all earthquakes were at depths of 2–16 km (Fig. 2). The focal depths ranged from 2 to 7, 5 to 10, 8 to 13, and 11 to 16 km in the first, second, third, and fourth groups, respectively (Table 1), which include 147, 327, 317, and 142 focal mechanisms, respectively. For the stress tensor inversion, we placed nodes horizontally in the study area with $0.1^\circ \times 0.1^\circ$ spacing. The inversion was carried out at each node using all events within an epicentral distance of 15 km from the node. Nodes with fewer than 10 events were only used to smooth gaps in the seismicity, and their results were not adopted. We selected the damping parameter e (equation (14) in Hardebeck and Michael (2006)) based on the trade-off curve between the model length and the data variance. The corner of the trade-off curve was near $e \approx 2$, so we selected $e = 2$ for all groups in this study.

Table 1 Results of stress inversion^a

Group	Depth	<i>N</i> of F.M.	<i>N</i> of nodes	σ_1 -axis	<i>R</i>
1st	2–7	147	25	N107°±5° E	0.7 ± 0.15
2nd	5–10	327	62	N100°±7° E	0.8 ± 0.12
3rd	8–13	317	58	N96°±9° E	0.9 ± 0.11
4th	11–16	142	33	N87°±8° E	0.8 ± 0.15

^aDepths are in km, *N* of F.M. is the number of focal mechanisms included in each group, and *N* of nodes is the number of nodes with more than 10 focal mechanisms

Results

Focal mechanisms

In the study area, the P-axes lie roughly in the E–W direction, and the T-axes are estimated to lie in the N–S direction (Fig. 4). The averages of the azimuths of the P- and T-axes are $N97^\circ \pm 23^\circ$ E and $N6^\circ \pm 32^\circ$ E, respectively, for all 597 focal mechanisms of quality A, B, and C (Fig. 4). The variance of the azimuths of the T-axes is larger than that of the P-axes. The averages of the dips of the P- and T-axes are $11^\circ \pm 10^\circ$ and $32^\circ \pm 25^\circ$, respectively. The P-axes are nearly horizontal, and the T-axes have a larger dip angle than the P-axes. The variance of the dips of the T-axes is larger than that of the P-axes. These variations of the P- and T-axes come from the variations in the focal mechanisms (Fig. 5). Triangle diagrams (Frohlich 2001) show the distribution of focal mechanisms based on the dip angles of the P-, T-, and N-axes. In the study area, we observed not only strike-slip earthquakes but also thrust-faulting earthquakes. Few normal fault earthquakes were observed.

Some earthquakes were triggered by the M9.0 Tohoku-Oki earthquake in March 2011, and some of these were even located outside of the focal area. Although the study area is located far from the focal area, a temporal change in the stress field may have occurred due to the Tohoku-Oki earthquake as well as a subsequent large afterslip. However, we found no clear temporal change in the azimuth and dip of P- and T-axes. Note that the higher number of focal mechanisms beginning around the beginning of 2011 was an apparent change. This change occurred because we detected the polarity of the first P-wave motion for all earthquakes larger than $M = 1.5$ before 2011, whereas after 2011, we detected the polarity for all earthquakes larger than $M = 1.0$.

Stress inversion

Figure 6 shows the direction of the maximum principal stress (σ_1) at each node. An additional data file shows the results in more detail (see Additional file 2). The average directions of the σ_1 -axes are $N107^\circ \pm 5^\circ$ E, $N100^\circ \pm 7^\circ$ E, $N96^\circ \pm 9^\circ$ E, and $N87^\circ \pm 8^\circ$ E for the first, second, third, and fourth groups, which have depths of 2–7, 5–10, 8–13, and 11–16 km, respectively (Table 1). The average direction rotates counterclockwise from ESE–WNW to ENE–WSW as the focal depth increases. This systematic rotation is affected mainly by a local fluctuation in the stress field around the Nobi fault system. In particular, the σ_1 -axis rotates clearly around the southern end of the seismic fault ruptured by the 1891 Nobi earthquake. However, rotation is not observed in the central part of the seismic fault of the 1891 event. This spatial pattern is most remarkable in the shallow portions at depths of 2–7 and 5–10 km, as shown in Fig. 6a, b, respectively, as opposed to the deep portions

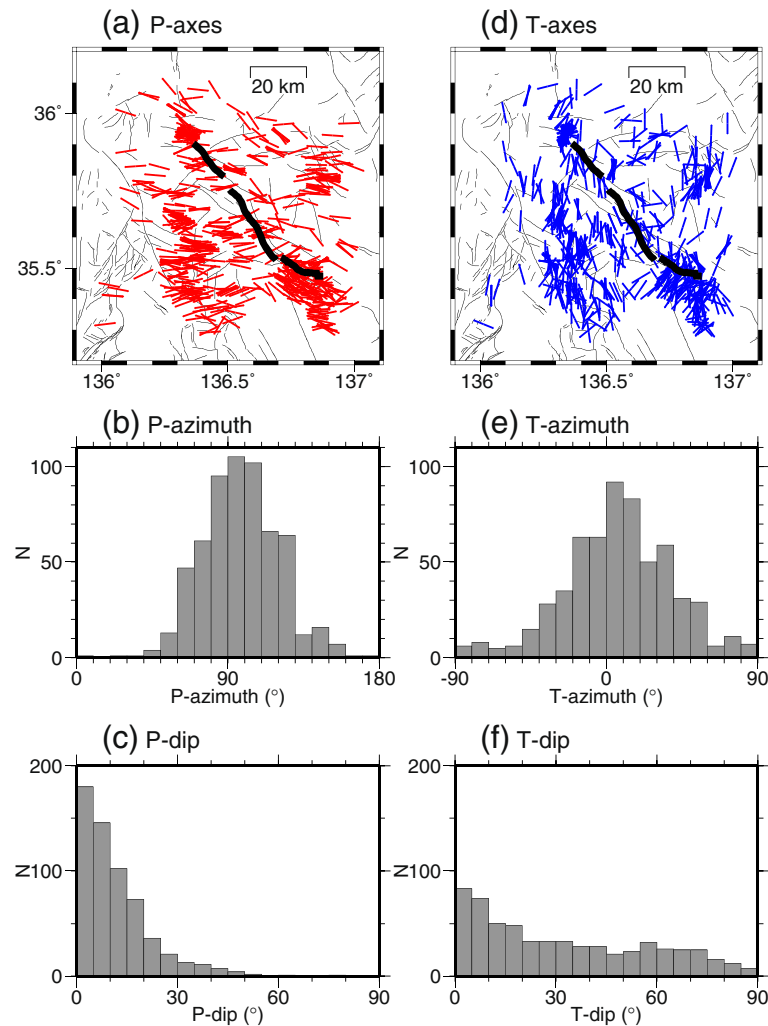


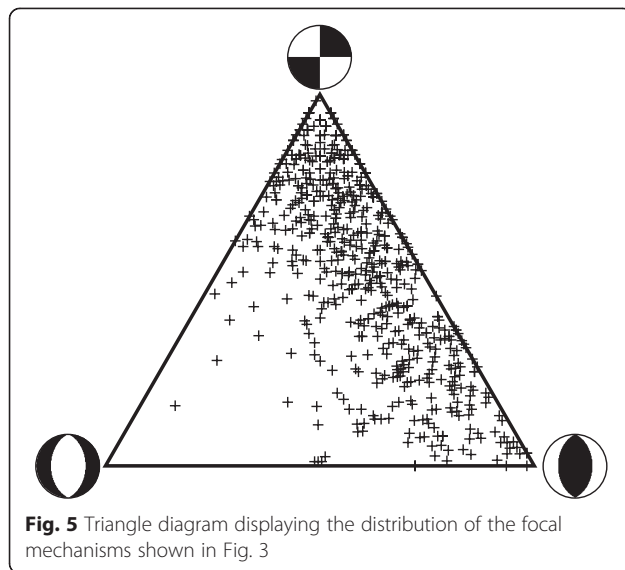
Fig. 4 Orientation of **a** P- and **d** T-axes of the focal mechanisms shown in Fig. 3. *Red lines* in **(a)** and *blue lines* in **(d)** indicate the strike of the P- and T-axes, respectively. *Bold lines* are the surface trace of the seismic fault ruptured by the 1891 Nobi earthquake. *Thin lines* are other active faults. Histograms of azimuths of **b** P- and **e** T-axes. Histograms of dip angles of **c** P- and **f** T-axes. 0° and 90° indicate horizontal and vertical axes, respectively

at depths of 8–13 and 11–16 km, as shown in Fig. 6c, d. Figure 7 shows the spatial change in the direction of the σ_1 -axis along the 35.7° N and 35.5° N lines of latitude. The 35.7° N line runs across the central part of the seismic fault ruptured by the 1891 Nobi earthquake, and the 35.5° N line runs across the southern end of the seismic fault. Along the 35.7° N line, no significant spatial change in the direction of the σ_1 -axis can be identified in the shallow or deep portions. Along the 35.5° N line, the σ_1 -axis in the shallow portion west of 136.5° E is oriented roughly E–W. Then, between 136.5° E and 136.9° E, the σ_1 -axis rotates clockwise by approximately 15°, and at approximately 137.0° E, it turns back to the original direction that it had west of 136.5° E.

The angle ϕ is defined as the angle between the σ_1 -axis and the strike of the fault. It is clear that the angle ϕ of

the Umehara fault is different from those of the other two segments at depths of 5–10 km. The strikes of the faults are as follows: N40° W for the Nukumi fault, N35° W for the Neodani fault, and N55° W for the Umehara fault. The direction of the σ_1 -axis applied to the Umehara fault is N70° W at (35.5° N, 136.8° E), and thus $\phi = 15^\circ$. On the other hand, the direction of the σ_1 -axis applied to the Neodani fault is N83° W at (35.7° N, 136.6° E), and thus $\phi = 48^\circ$. The direction of the σ_1 -axis applied to the Nukumi fault is N79° W at (35.8° N, 136.5° E), and thus $\phi = 39^\circ$.

The focal mechanisms also change in the shallow portion (Fig. 7). Whereas the numbers of strike-slip and reverse faults are approximately the same west of 136.5° E, the number of reverse faults decreases between 136.5° E and 136.9° E. The surface trace of the seismic fault



ruptured by the 1891 Nobi earthquake is located around 136.7°E – 136.8°E . This strongly suggests that the 15° rotation between 136.5°E and 136.9°E is related to a tectonic process of the Nobi fault system. Although we focus on the stress variation at the southern end of the

fault in the following discussion, the σ_1 -axes in the northern part of the study area above latitude 35.8°N appear to be oriented entirely ESE–WNW.

The stress ratio R , which is defined as $R = (\sigma_1 - \sigma_2) / (\sigma_1 - \sigma_3)$, is shown in Fig. 8 and Table 1. The stress ratio R ranges from 0.65–0.98, and the average R over the study area is 0.82. The stress ratios are close to unity, indicating $\sigma_2 \approx \sigma_3$. It is natural to assume that the vertical stress is close to the lithostatic stress or the overburden pressure. Thus, we interpret these results to indicate that σ_2 and σ_3 are equal to the lithostatic stress in the study area. In the central and southeastern parts of the seismic fault ruptured by the 1891 Nobi earthquake, the stress ratio R is approximately 0.7, 0.8, and 0.9 at depths of 2–7, 5–10, and 8–13, respectively, indicating that R increases as the depth increases. However, the error in R estimated using the bootstrap method is approximately 0.15; thus, we conclude that no significant spatial change is identified in either the horizontal or depth direction.

Discussion

We find that (1) both strike-slip and reverse fault earthquakes are observed in the study area, (2) the σ_1 -axis is oriented E–W or ESE–WNW, and (3) the stress ratio is

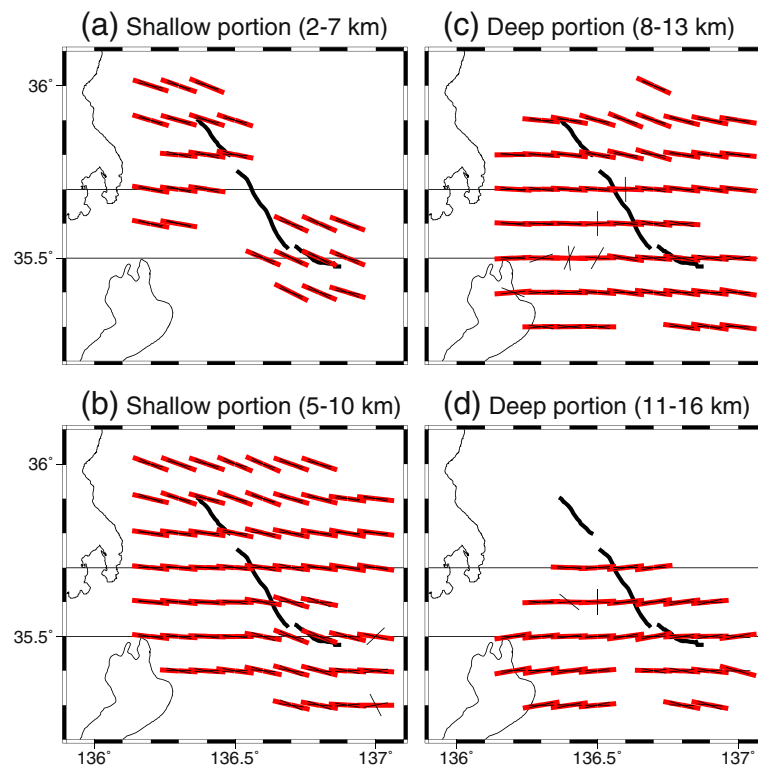


Fig. 6 Inverted maximum principal stress σ_1 in the Nobi fault area. An additional data file shows the results in more detail (see Additional file 2). One red and two black lines at each grid point indicate the azimuth of σ_1 and the range of estimation error, respectively. Bold black lines show the seismic fault ruptured by the 1891 Nobi earthquake. The 35.5°N and 35.7°N lines of latitude are drawn. The stress tensor inversion was conducted in the four layers with depths of **a** 2–7 km, **b** 5–10 km, **c** 8–13 km, and **d** 11–16 km

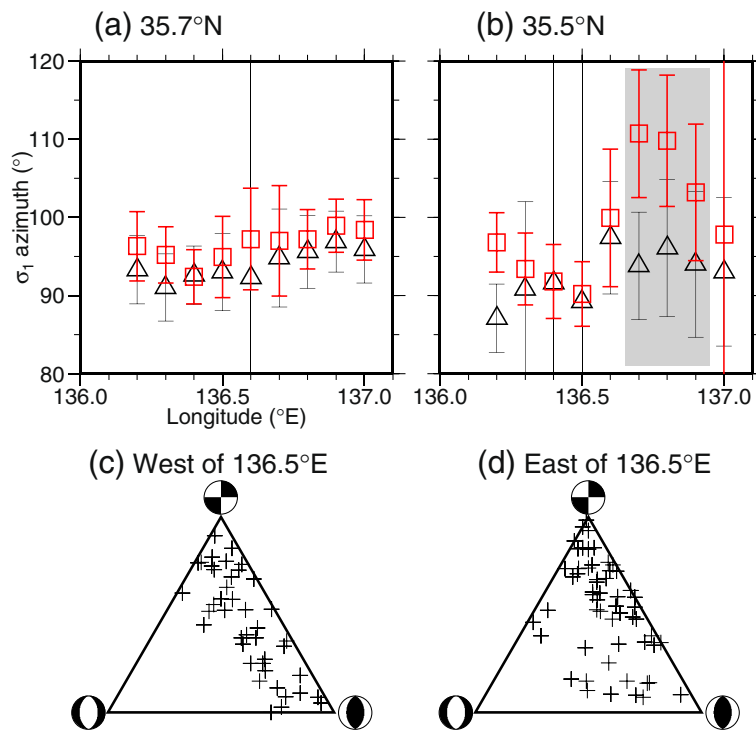


Fig. 7 Spatial change in the direction of the σ_1 -axis along the **a** 35.7° N and **b** 35.5° N lines of latitude. Shaded area in **(b)** shows the zone of rotation of the σ_1 -axis. Rectangles and triangles indicate the direction in the layers with depths of 5–10 km and 8–13 km, respectively. **(c)** Focal mechanisms used for the stress inversion at (35.5° N, 136.3° E) and (35.5° N, 136.4° E). **d** Focal mechanisms used for the stress inversion at (35.5° N, 136.7° E) and (35.5° N, 136.8° E)

close to 1.0, indicating $\sigma_2 \approx \sigma_3$. Townsend and Zoback (2006) investigated the spatial pattern of the stress field at a regional scale all over Japan and found that the axis of greatest horizontal compressive stress is oriented ESE–WNW west of approximately 136° E in central Japan, which is consistent with our results. Terakawa and Matsu'ura (2010) found that compressional stress is dominant in central Japan and that its axis is oriented E–W, which is also consistent with our results. Tsutsumi et al. (2012) inverted 169 fault-slip data points from 37 active faults in the eastern part of the Southwest Japan arc, including the Nobi fault area. They found that the direction of the σ_1 -axis tends to be ESE–WNW and that the stress ratio is close to 1.0, indicating $\sigma_2 \approx \sigma_3$, which suggests that the stress field in central Japan has been uniform and stable over the past approximately 10^5 years. The direction of the σ_1 -axis and the stress ratio obtained by Tsutsumi et al. (2012) are consistent with the results in this study. Hiramatsu and Iidaka (2015) obtained a spatial distribution of *S*-wave splitting parameters and found that the observed polarization orientation ranges from E–W to NW–SE, which is consistent with the direction of the σ_1 -axis obtained in this study.

As mentioned above, the stress field obtained in this study is in very good agreement with the results of

previous studies except for the local fluctuation obtained in the southwestern part of the Nobi fault system. The direction of the σ_1 -axis changes steeply in the narrow zone south of 35.6° N at depths shallower than ~10 km. Kato et al. (2006) observed rotation of the σ_1 -axis around the southwestern end of the aftershock area of the 2004 mid-Niigata prefecture (M_w 6.6) earthquake, and they suggested that the rotation of the σ_1 -axis might be caused by the lateral variation of low-velocity bodies in the hanging wall. In the case of the Nobi fault system, however, the *P*- and *S*-wave velocity structures in the local fluctuation area appear to be the same as those of other areas along the Nobi fault system (Nakajima et al. 2014). The spatial distribution of coda *Q* is also uniform along the entire Nobi fault system (Tsuji et al. 2014). Therefore, the local fluctuation of the σ_1 -axis may not be caused by differences in the crustal structure. Fujino and Katao (2009) also reported a sharp change in the stress field across the Hanaori fault, which is located near the western boundary of the study area, and they presented no hypothesis to explain the sharp change in the stress field.

Hardebeck and Hauksson (2001) calculated $\Delta\theta$ as a function of θ , where θ is the angle between a seismic fault and the direction of the σ_1 -axis applied to the

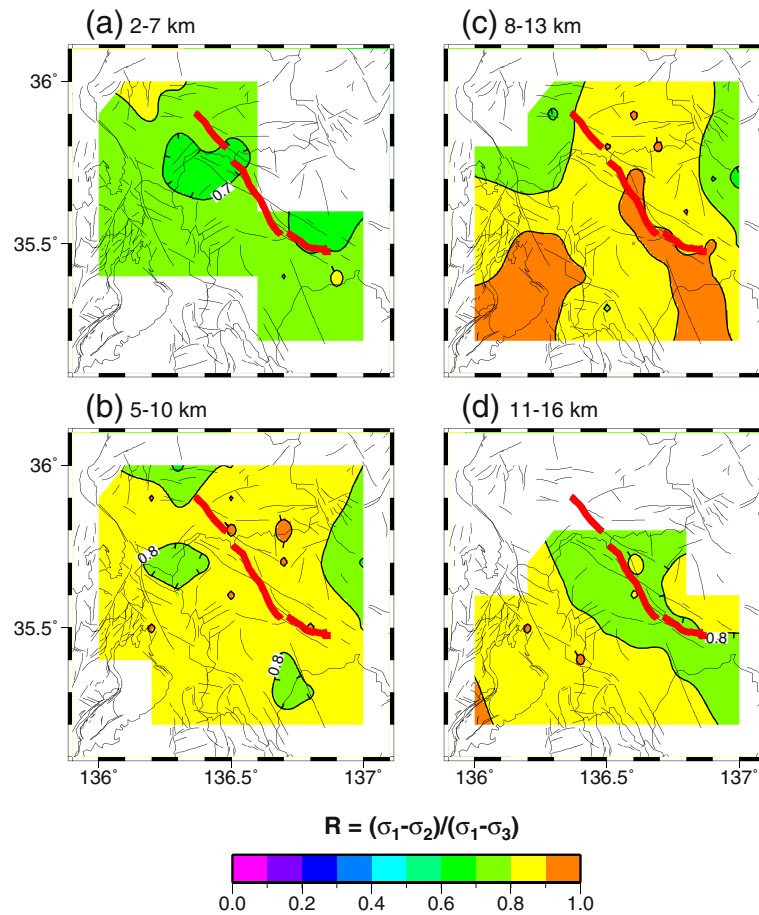


Fig. 8 Distribution of the stress ratio in the four layers with depths of **a** 2–7 km, **b** 5–10 km, **c** 8–13 km, and **d** 11–16 km. Bold red lines are the surface trace of the seismic fault ruptured by the 1891 Nobi earthquake. Thin black lines are other active faults

seismic fault before an earthquake and $\Delta\theta$ is the rotation angle of the σ_1 -axis due to the occurrence of an earthquake. Based on this model, we are able to present a hypothesis that explains the local fluctuation of the σ_1 -axis found in this study. Although we stated in the introduction that the stress accumulation process for intraplate regions is still under debate, we assume that local stress accumulation occurs near the source fault. Before the 1891 Nobi earthquake occurred, the σ_1 -axis may have been oriented roughly NW–SE, rather than E–W, along the entire Nobi fault ruptured by the 1891 event, indicating that the deviatoric stress accumulated in the narrow zone along the entire Nobi fault. Thus, we assumed that the σ_1 -axis was oriented N70° W before the 1891 Nobi earthquake occurred, which is the present orientation of the σ_1 -axis at (35.5° N, 136.8° E) obtained by the stress inversion at the depth of 5–10 km. The strikes of the faults are N40° W for the Nukumi fault, N35° W for the Neodani fault, and N55° W for the Umehara fault; therefore, θ for the model by Hardebeck and Hauksson (2001) is equal to 30° for the Nukumi fault, 35° for the

Neodani fault, and 15° for the Umehara fault. When the 1891 Nobi earthquake occurred, the σ_1 -axis rotated from N70° W to N83° W in the central segment of the Nobi fault, where the stress drop may have been very large. The N83° W direction is the present orientation of the σ_1 -axis at (35.7° N, 136.6° E) in the Neodani fault obtained by the stress inversion at the depth of 5–10 km. In this case, $\Delta\theta = -13^\circ$ for the Neodani fault, and thus approximately 70 % of the deviatoric stress was released based on the model by Hardebeck and Hauksson (2001). However, the rotation of the σ_1 -axis was very small, that is, $\Delta\theta = 0^\circ$, and the N70° W direction of the σ_1 -axis was maintained at the southern end of the seismic fault due to the small stress drop, indicating that most of the deviatoric stress around the Umehara fault was not released by the 1891 event. Fukuyama and Mikumo (2006) presented evidence supporting the assumption of the stress drop distribution, and they found that the static stress drop was 3.6–12.9 MPa in the central part of the seismic fault ruptured by the 1891 Nobi earthquake and 1.8–3.6 MPa in and around its southern end. Takano

and Kimata (2013) reevaluated the fault-slip model based on geodetic survey data and found that the coseismic horizontal displacement was 4.2–7.3 m in the central part and 2.0–3.8 m in and around the southern end, which also supports our assumption. The hypothesis that the deviatoric stress was not released at the southern end of the fault, based on the model by Hardebeck and Hauksson (2001), depends strongly on the direction of the σ_1 -axis prior to the mainshock. Therefore, the assumption that the σ_1 -axis was oriented N70° W before the Nobi earthquake must be validated based on more compelling evidence to determine whether this hypothesis is correct. The 2011 Tohoku-Oki (M_w 9.0) earthquake is another reliable example of the release of almost all deviatoric stress (Hasegawa et al. 2012). In this case, a coseismic rotation of the principal stress axis was clearly observed. However, no coseismic rotation of the principal stress axis was observed as a result of the 2000 western Tottori (M_w 6.6) earthquake (Yukutake et al. 2007). In this case, it is likely that only a small amount of the deviatoric stress was released by the mainshock.

The strike of the Umehara fault in the area of the spatial stress rotation is different from the strike of the other two faults in the central part ruptured by the 1891 Nobi earthquake. Additionally, a buried fault, a reverse fault dipping to the east, located to the southwest of the Umehara fault might have been ruptured by the 1891 Nobi earthquake (Kuriyama et al. 2013). Therefore, an alternative hypothesis is that the spatial rotation of the σ_1 -axis is related to the change of strike or/and the rupture of the buried fault.

Conclusions

We obtained 728 focal mechanisms of small earthquakes in the Nobi fault area in central Japan. The averages of the azimuths of the P- and T-axes are $N97^\circ \pm 23^\circ$ E and $N6^\circ \pm 32^\circ$ E, respectively. The P-axes are nearly horizontal, and the T-axes have a larger dip than the P-axes. We observed both strike-slip and reverse fault earthquakes in the study area. Few normal fault earthquakes were observed. The focal mechanisms were applied to a stress tensor inversion method to investigate the stress field and its spatial pattern. We found that over the entire study area, the σ_1 -axis is oriented E–W. However, the spatial pattern of the σ_1 -axis fluctuated locally at the southeastern end of the seismic fault ruptured by the 1891 Nobi earthquake. This local fluctuation suggests that most of the deviatoric stress at the southern end of the seismic fault was not released. However, this hypothesis depends strongly on the direction of σ_1 -axis prior to the 1891 Nobi earthquake. Therefore, the assumption that the σ_1 -axis was oriented NW–SE before the Nobi

earthquake must be validated based on more compelling evidence to determine whether the hypothesis is correct.

Additional files

Additional file 1: Focal mechanisms determined in this study. We used the HASH program (Hardebeck and Shearer 2002).

Additional file 2: Results of a stress tensor inversion. We used the Spatial And Temporal Stress Inversion (SATSI) method developed by Hardebeck and Michael (2006).

Competing interests

The authors declare that they have no competing interests.

Authors' contributions

KK wrote the first manuscript. All authors made substantial contributions to the data analysis and the deployment of the temporary seismic stations used in this study. All authors read and approved the final manuscript.

Acknowledgements

This study was supported by the Ministry of Education, Culture, Sports, Science and Technology (MEXT) of Japan, under its Earthquake and Volcano Hazards Observation and Research Program. We used data from JMA and Hi-net/NIED. We thank A. Nishizawa, who is an editor of this journal, and two anonymous reviewers for valuable comments. GMT-SYSTEM (Wessel and Smith 1991) was used for data mapping. To determine focal mechanism solutions, we used the program HASH produced by Hardebeck and Shearer (2002). To conduct the stress tensor inversion, we used the program SATSI developed by Hardebeck and Michael (2006).

Author details

¹Institute of Seismology and Volcanology, Hokkaido University, Sapporo 060-0810, Japan. ²Earthquake and Volcano Observatory, Hirosaki University, Hirosaki, Japan. ³Disaster Prevention Research Institute, Kyoto University, Kyoto, Japan. ⁴Earthquake and Volcano Research Center, Nagoya University, Nagoya, Japan. ⁵Present address: Faculty of Science, Ibaraki University, Mito, Japan.

Received: 4 March 2015 Accepted: 16 June 2015

Published online: 25 June 2015

References

- Awata Y, Kariya Y, Okumura K (1999) Segmentation of the surface ruptures associated with the 1891 Nobi earthquake, Central Honshu, Japan, based on the paleoseismic investigations. Interim Report on Active Fault and Paleoseismic Researches in the 1998 Fiscal Year: 115–130.
- Campbell DL (1978) Investigation of the stress-concentration mechanism for intraplate earthquakes. *Geophys Res Lett* 5:477–479
- Frohlich C (2001) Display and quantitative assessment of distributions of earthquake focal mechanisms. *Geophys J Int* 144:300–308
- Fujino H, Katao H (2009) Focal mechanism and regional stress field around the Biwako-seigan fault system (in Japanese). *Annuals Disas Prev Inst Kyoto Univ* No 52B:275–284
- Fukuyama E, Mikumo T (2006) Dynamic rupture propagation during the 1891 Nobi, Central Japan, earthquake: a possible extension to the branched faults. *Bull Seismol Soc Am* 96:1257–1266. doi:10.1785/0120050151
- Fukuyama E, Muramatsu I, Mikumo T (2007) Seismic moment of the 1891 Nobi, Japan, earthquake estimated from historical seismograms. *Earth Planets Space* 59:553–559
- Hardebeck JL, Hauksson E (2001) Crustal stress field in southern California and its implications for fault mechanics. *J Geophys Res* 106:21859–21882
- Hardebeck JL, Michael AJ (2006) Damped regional-scale stress inversions: Methodology and examples for southern California and the Coalinga aftershock sequence. *J Geophys Res* 111, B11310. doi:10.1029/2005JB004144
- Hardebeck JL, Shearer PM (2002) A new method for determining first-motion focal mechanisms. *Bull Seismol Soc Am* 92:2264–2276

- Hasegawa A, Yoshida K, Asano Y, Okada T, Iinuma T, Ito Y (2012) Change in stress field after the 2011 great Tohoku-Oki earthquake. *Earth Planet Sci Lett* 355–356:231–243
- Hinze WJ, Braille LW, Keller GR, Lidiak EG (1988) Models for mid-continent tectonism: an update. *Rev Geophys* 26:699–717
- Hiramatsu Y, Iidaka T, The Research Group for the Joint Seismic Observations at the Nobi Area (2015) Stress state in the upper crust around the source region of the 1891 Nobi earthquake through shear wave polarization anisotropy. *Earth Planets Space* 67:52
- Hirata N, Matsu'ura M (1987) Maximum-likelihood estimation of hypocenter with origin time eliminated using nonlinear inversion technique. *Phys Earth Planet Inter* 47:50–61
- Ito K, Wada H (2002) Observation of microearthquakes in the Atotsugawa fault region, central Honshu, Japan. In: Yanagidani T, Ando M (eds) Ogasawara H. A. A. Balkema Publishers, Seismogenic Process Monitoring, pp 229–243
- Johnston AC, Kanter LR (1990) Earthquakes in stable continental crust. *Sci Am* 262(3):68–75
- Kato A, Sakai S, Hirata N, Kurashimo E, Iidaka T, Iwadaki T, Kanazawa T (2006) Imaging the seismic structure and stress field in the source region of the 2004 mid-Niigata prefecture earthquake: Structural zones of weakness and seismogenic stress concentration by ductile flow. *J Geophys Res* 111, B08308. doi:10.1029/2005JB004016
- Kawanishi R, Iio Y, Yukutake Y, Shibutani T, Katao H (2009) Local stress concentration in the seismic belt along the Japan Sea coast inferred from precise focal mechanisms: Implications for the stress accumulation process on intraplate earthquake faults. *J Geophys Res* 114, B01309. doi:10.1029/2008JB005765
- Kuriyama M, Sato H, Iwata T (2013) Examination of source fault model for the Gifu-Ichinomiya fault based on seismic intensity data. *Earth Planets Space* 65:1449–1462
- Liu L, Zoback MD (1997) Lithospheric strength and intraplate seismicity in the New Madrid seismic zone. *Tectonics* 16:585–595
- Matsuda T (1974) Surface faults associated with Nobi (Mino-Owari) earthquake of 1891, Japan. *Spec Rep Earthq Res Inst* 13:85–126
- Michael AJ (1987) Use of focal mechanisms to determine stress: a control study. *J Geophys Res* 92:357–368
- Milne J (1893) A note on the great earthquake of October 28th 1891. *J Seismol Soc Jpn* 17:127–151
- Nakajima J, Kato A, Iwasaki T, The Research Group for the Joint Seismic Observations at the Nobi Area (2014) The weakened lower crust beneath the Nobi fault system, Japan: Implications for stress accumulation process to the seismogenic layer. *Tectonophysics*: in print.
- Stuart WD, Hildenbrand TG, Simpson RW (1997) Stressing of the New Madrid seismic zone by a lower crust detachment fault. *J Geophys Res* 102:27,623–27,633
- Sykes LR (1978) Intraplate seismicity, reactivation of preexisting zones of weakness, alkaline magmatism, and other tectonism postdating continental fragmentation. *Rev Geophys* 16:621–688
- Takano K, Kimata F (2013) Reexamination of the fault slip model of the 1891 M 8.0 Nobi earthquake: the first earthquake detected by a geodetic survey in Japan. *Earth Planets Space* 65:935–941
- Terakawa T, Matsu'ura M (2010) The 3-D tectonic stress fields in and around Japan inverted from centroid moment tensor data of seismic events. *Tectonics* 29, TC6008. doi:10.1029/2009TC002626
- Townend J, Zoback MD (2006) Stress, strain, and mountain building in central Japan. *J Geophys Res* 111, B03411. doi:10.1029/2005JB003759
- Tsuji S, Hiramatsu Y, The Japanese University Group of the Joint Seismic Observations at the Area of Nobi Earthquake (2014) Spatial variation in coda Q around the Nobi fault zone, central Japan: relation to S-wave velocity and seismicity. *Earth Planets Space* 66:97
- Tsutsumi H, Sato K, Yamaji A (2012) Stability of the regional stress field in central Japan during the late Quaternary inferred from the stress inversion of the active fault data. *Geophys Res Lett* 39, L23303. doi:10.1029/2012GL054094
- Wessel P, Smith WHF (1991) Free software helps map and display data. *Eos Trans AGU* 72:445–446
- Yukutake Y, Iio Y, Katao H, Shibutani T (2007) Estimation of the stress field in the region of the 2000 western Tottori earthquake: using numerous aftershock focal mechanisms. *J Geophys Res* 112, B09306. doi:10.1029/2005JB004250
- Zoback ML (1992) Stress field constraints on intraplate seismicity in eastern North America. *J Geophys Res* 97:11,761–11,782

Submit your manuscript to a SpringerOpen[®] journal and benefit from:

- Convenient online submission
- Rigorous peer review
- Immediate publication on acceptance
- Open access: articles freely available online
- High visibility within the field
- Retaining the copyright to your article

Submit your next manuscript at ► springeropen.com